

Journal of Materials Chemistry A

Accepted Manuscript



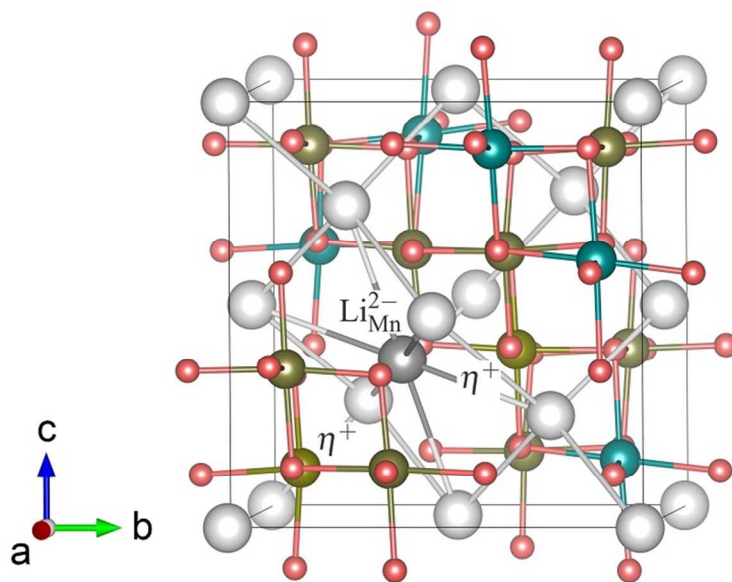
This is an *Accepted Manuscript*, which has been through the Royal Society of Chemistry peer review process and has been accepted for publication.

Accepted Manuscripts are published online shortly after acceptance, before technical editing, formatting and proof reading. Using this free service, authors can make their results available to the community, in citable form, before we publish the edited article. We will replace this *Accepted Manuscript* with the edited and formatted *Advance Article* as soon as it is available.

You can find more information about *Accepted Manuscripts* in the [Information for Authors](#).

Please note that technical editing may introduce minor changes to the text and/or graphics, which may alter content. The journal's standard [Terms & Conditions](#) and the [Ethical guidelines](#) still apply. In no event shall the Royal Society of Chemistry be held responsible for any errors or omissions in this *Accepted Manuscript* or any consequences arising from the use of any information it contains.

Spinel-type LiMn_2O_4 is prone to lithium over-stoichiometry in which a certain amount of lithium ions occupy the manganese sites.



Understanding the electronic and ionic conduction and lithium over-stoichiometry in LiMn_2O_4 spinel

Khang Hoang*

Received Xth XXXXXXXXXXXX 2014, Accepted Xth XXXXXXXXXXXX 2014

First published on the web Xth XXXXXXXXXXXX 2014

DOI: 10.1039/b000000x

We report a first-principles study of defect thermodynamics and transport in spinel-type lithium manganese oxide LiMn_2O_4 , an important lithium-ion battery electrode material, using density-functional theory and the Heyd-Scuseria-Ernzerhof screened hybrid functional. We find that intrinsic point defects in LiMn_2O_4 have low formation energies and hence can occur with high concentrations. The electronic conduction proceeds via hopping of small polarons and the ionic conduction occurs via lithium vacancy and/or interstitial migration mechanisms. The total conductivity is dominated by the electronic contribution. LiMn_2O_4 is prone to lithium over-stoichiometry, *i.e.*, lithium excess at the manganese sites, and $\text{Mn}^{3+}/\text{Mn}^{4+}$ disorder. Other defects such as manganese antisites and vacancies and lithium interstitials may also occur in LiMn_2O_4 samples. In light of our results, we discuss possible implications of the defects on the electrochemical properties and provide explanations for the experimental observations and guidelines for defect-controlled synthesis and defect characterization.

1 Introduction

Spinel-type LiMn_2O_4 , a mixed-valent compound containing both Mn^{3+} and Mn^{4+} ions, has been considered as an alternative to layered LiCoO_2 for lithium-ion battery electrodes as manganese is inexpensive and environmentally benign compared to cobalt in the layered oxide.^{1,2} The material crystallizes in the cubic crystal structure of space group $Fd\bar{3}m$ at room temperature but transforms into an orthorhombic or tetragonal structure at lower temperatures. In the cubic phase, the Li^+ ions stay at the tetrahedral 8a sites of the cubic close-packed oxygen array, whereas the Mn^{3+} and Mn^{4+} ions randomly occupy the octahedral 16d sites. In the orthorhombic or tetragonal phase, the $\text{Mn}^{3+}/\text{Mn}^{4+}$ arrangement is believed to be charge-ordered.^{3–9} However, truly stoichiometric LiMn_2O_4 is hard to obtain in experiments and intrinsic electronic and ionic defects appear to occur at multiple lattice sites.^{9–15} In fact, LiMn_2O_4 samples are often made lithium over-stoichiometric (*i.e.*, Li-excess), intentionally or unintentionally.^{13–22} The total bulk conductivity of LiMn_2O_4 has also been reported and thought to be predominantly from hopping of polarons.^{22–24} A deeper understanding of these properties and observations clearly requires a detailed understanding of the defect thermodynamics and transport. Such an understanding is currently lacking.

Computational studies of LiMn_2O_4 have focused mainly

on the bulk properties and lithium and small polaron migration,^{25–30} except for some studies of defect energetics by Amundsen *et al.*³⁰ using interatomic potential simulations and Koyama *et al.*³¹ using density-functional theory (DFT) within the local density approximation (LDA).³² First-principles calculations based on DFT have been proven to be a powerful tool for addressing electronic and atomistic processes in solids. A comprehensive and systematic DFT study of intrinsic point defects in a battery electrode material, for example, can provide a detailed picture of the defect formation and migration and invaluable insights into the electrochemical performance.^{33,34} For LiMn_2O_4 , such a study is quite challenging, partly because standard DFT calculations using LDA or the generalized-gradient approximation (GGA)³⁵ fail to produce the correct physics of even the host compound. LDA/GGA calculations carried out by Mishra and Ceder,³⁶ *e.g.*, showed that LiMn_2O_4 is a metal with a Mn oxidation state of +3.5, which is in contrast to what is known about LiMn_2O_4 as a material with a finite band gap and mixed Mn^{3+} and Mn^{4+} ions. The GGA+*U* method,^{37,38} an extension of GGA, can give a reasonable electronic structure. However, since one has to assume that the transition metal has the same Hubbard *U* value in different chemical environments, the transferability of GGA+*U* results across the compounds is low, making defect calculations become inaccurate.

In this article, we present for the first time a comprehensive study of electronic and ionic defects in LiMn_2O_4 using a hybrid Hartree-Fock/DFT method. In particular, we used

Center for Computationally Assisted Science and Technology, North Dakota State University, Fargo, ND 58108, USA. E-mail: khang.hoang@ndsu.edu

the Heyd-Scuseria-Ernzerhof (HSE06)^{39,40} screened hybrid functional where all orbitals are treated on the same footing. The atomic and electronic structure and phase stability of the host compound and the structure and energetics of all possible intrinsic point defects were investigated; the migration of selected defects was also explored. We find that defects in LiMn₂O₄ have low formation energies and hence can occur with high concentrations, and lithium antisites are the dominant ionic defect. On the basis of our results, we discuss the Mn³⁺/Mn⁴⁺ disorder, electronic and ionic conduction, delithiation and lithiation mechanisms, lithium over-stoichiometry, and possible implications on the electrochemical properties. Ultimately, our work provides explanations for the experimental observations, guidelines for defect characterization and defect-controlled synthesis, and insights for rational design of LiMn₂O₄-based electrode materials with improved performance.

2 Methodology

2.1 Computational details

Our calculations were based on DFT, using the HSE06 hybrid functional,^{39,40} the projector augmented wave method,^{41,42} and a plane-wave basis set, as implemented in the VASP code.^{43–45} Point defects were treated within the supercell approach, in which a defect is included in a finite volume of the host material and this structure is periodically repeated. For bulk and defect calculations, we mainly used supercells of LiMn₂O₄ containing 56 atoms/cell; integrations over the Brillouin zone were carried out using a 2×2×2 Monkhorst-Pack **k**-point mesh.⁴⁶ A denser, Γ -centered 4×4×4 **k**-point mesh was used in calculations to produce the electronic density of states. The plane-wave basis-set cutoff was set to 500 eV. Convergence with respect to self-consistent iterations was assumed when the total energy difference between cycles was less than 10⁻⁴ eV and the residual forces were less than 0.01 eV/Å. In the defect calculations, which were performed with spin polarization and the ferromagnetic spin configuration, the lattice parameters were fixed to the calculated bulk values but all the internal coordinates were fully relaxed.

2.2 Defect formation energies

The key quantities that determine the properties of a defect are the migration barrier and formation energy. In our calculations, the former is calculated by using climbing-image nudged elastic-band (NEB) method;⁴⁷ the latter is computed using the total energies from DFT calculations. Following the approach described in Ref.³⁴ and references therein, the for-

mation energy of a defect X in charge state q is defined as

$$E^f(X^q) = E_{\text{tot}}(X^q) - E_{\text{tot}}(\text{bulk}) - \sum_i n_i \mu_i + q(E_v + \mu_e) + \Delta^q, \quad (1)$$

where $E_{\text{tot}}(X^q)$ and $E_{\text{tot}}(\text{bulk})$ are, respectively, the total energies of a supercell containing the defect X and of a supercell of the perfect bulk material; μ_i is the atomic chemical potential of species i (and is referenced to bulk metals or O₂ molecules at 0 K), and n_i indicates the number of atoms of species i that have been added ($n_i > 0$) or removed ($n_i < 0$) to form the defect. μ_e is the electronic chemical potential, referenced to the valence-band maximum in the bulk (E_v). Δ^q is the correction term to align the electrostatic potentials of the bulk and defect supercells and to account for finite-cell-size effects on the total energies of charged defects.⁴⁸ To correct for the finite-size effects, we adopted the approach of Freysoldt *et al.*,^{49,50} in which Δ^q was determined using a calculated static dielectric constant of 11.02 for LiMn₂O₄. The dielectric constant was computed following the procedure described in Ref.³⁴ according to which the electronic contribution was obtained in HSE06 calculations whereas the ionic contribution was obtained in GGA+ U with $U=4.84$ eV for Mn, taken as an average value of Mn³⁺ (4.64 eV) and Mn⁴⁺ (5.04 eV).⁵¹

In eqn (1), the atomic chemical potentials μ_i can describe experimental conditions and are subject to various thermodynamic constraints.^{34,48} The stability of LiMn₂O₄, for example, requires

$$\mu_{\text{Li}} + 2\mu_{\text{Mn}} + 4\mu_{\text{O}} = \Delta H^f(\text{LiMn}_2\text{O}_4), \quad (2)$$

where ΔH^f is the formation enthalpy. There are other constraints imposed by competing Li–Mn–O phases. By taking into account all these thermodynamic constraints, one can determine the range of Li, Mn, and O chemical potential values in which the host compound LiMn₂O₄ is thermodynamically stable. The oxygen chemical potential, μ_{O} , can also be related to the temperatures and pressures through standard thermodynamic expressions for O₂ gas.³³ Finally, the electronic chemical potential μ_e , *i.e.*, the Fermi level, is not a free parameter but subject to the charge neutrality condition that involves all possible intrinsic defects and any impurities in the material.^{34,48}

The concentration of a defect at temperature T is related to its formation energy through the expression⁴⁸

$$c = N_{\text{sites}} N_{\text{config}} \exp\left(\frac{-E^f}{k_B T}\right), \quad (3)$$

where N_{sites} is the number of high-symmetry sites in the lattice per unit volume on which the defect can be incorporated, N_{config} is the number of equivalent configurations (per site), and k_B is the Boltzmann constant. Strictly speaking, this expression is only valid in thermodynamic equilibrium. Materials synthesis, on the other hand, may not be an equilibrium

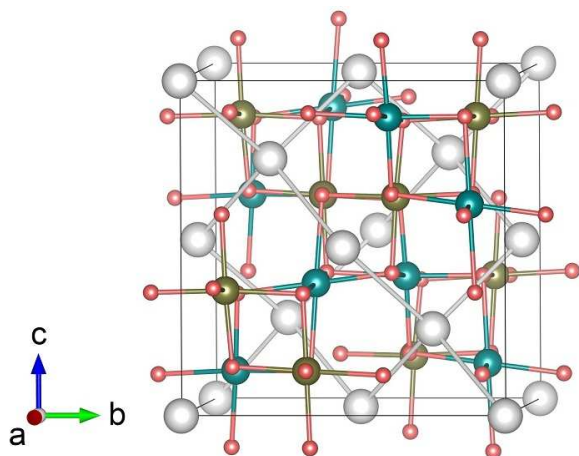


Fig. 1 Supercell model for spinel-type LiMn_2O_4 after structural optimization. Large gray spheres are Li, medium blue (yellow) spheres are Mn^{3+} (Mn^{4+}), and small red spheres are O.

process. However, even in that case the use of the equilibrium expression can still be justified if the synthesis conditions are close enough to equilibrium. Besides, as discussed in Ref. ⁴⁸, the use of eqn (3) does not require that all aspects of the process have to be in equilibrium. What is important is that the relevant defects are mobile enough to allow for equilibration at the temperatures of interest. It emerges from eqn (3) that defects with low formation energies will easily form and occur in high concentrations.

3 Results

3.1 Bulk properties

We began with a cubic supercell of LiMn_2O_4 (space group $Fd\bar{3}m$, experimental lattice parameter $a = 8.24 \text{ \AA}$),⁵² consisting of 8 Li atoms at the 8a sites, 16 Mn atoms at the 16d sites, and 32 O atoms at the 32e sites; the interstitial 16c sites are left empty. After structural optimization, this cubic cell transforms into a tetragonally distorted cell with $a = c = 8.34 \text{ \AA}$ and $b = 8.11 \text{ \AA}$; see Fig. 1. The ordering of $\text{Mn}^{3+}/\text{Mn}^{4+}$ is visible in the relaxed structure. If viewed along the [101] direction, the atomic arrangement follows an A–B–C–... pattern with layer A consisting of Mn^{3+} chains, B of Li^+ chains and $\text{Mn}^{3+}/\text{Mn}^{4+}$ -alternating chains, and C of Mn^{4+} chains. The Mn ions are stable in high-spin states with calculated magnetic moments of $3.78 \mu_B$ (Mn^{3+}) and $3.04 \mu_B$ (Mn^{4+}). There are six Mn^{4+} –O bonds with similar bond lengths (1.85 – 1.93 \AA), four short Mn^{3+} –O bonds (1.92 – 1.98 \AA), and two long Mn^{3+} –O bonds (2.20 \AA). The local distortions as seen in Fig. 1 are thus due to Jahn-Teller effects associated with the Mn^{3+} ions.

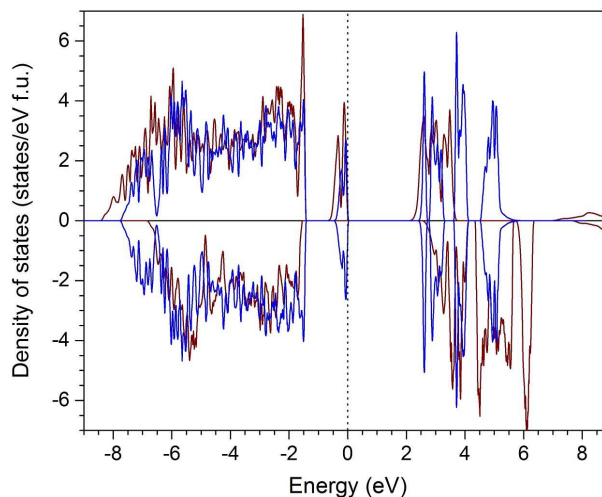


Fig. 2 Electronic density of states of LiMn_2O_4 in antiferromagnetic (blue curves) and ferromagnetic (red curves) spin configurations. The zero of energy is set to the highest occupied state.

Among several different $\text{Mn}^{3+}/\text{Mn}^{4+}$ arrangements we investigated, the described model is found to have the lowest energy. It is lower in energy than the second-lowest energy $\text{Mn}^{3+}/\text{Mn}^{4+}$ arrangement by 0.06 eV per formula unit (f.u.), and the LiMn_2O_4 supercell where every Mn ion has an oxidation state of $+3.5$ by 0.47 eV/f.u. Our results are thus consistent with experimental reports showing a transformation into a tetragonal or orthorhombic phase at low temperatures associated with charge ordering.^{3–9} We use this structural model for further studies of the bulk properties and for defect calculations (see below). Since the above mentioned global and local distortions are relatively small, the atomic positions in this model will be nominally referred to using the Wyckoff positions of the cubic structure.

Figure 2 shows the total electronic density of states of LiMn_2O_4 . An analysis of the wavefunctions shows that the valence-band maximum (VBM) predominantly consists of the 3d states from the Mn^{3+} sites, whereas the conduction-band minimum (CBM) are predominantly the 3d states from the Mn^{4+} sites. The Li 2s state is high up in the conduction band, indicating that Li donates its electron to the lattice and becomes Li^+ . LiMn_2O_4 thus can be regarded nominally as an ordered arrangement of Li^+ , Mn^{3+} , Mn^{4+} , and O^{2-} units. The calculated band gaps are 2.12 and 2.42 eV for the ferromagnetic (FM) and antiferromagnetic (AFM) configurations, respectively. In addition to the spin configurations, we find that the calculated band gap of LiMn_2O_4 also depends on the $\text{Mn}^{3+}/\text{Mn}^{4+}$ arrangement. For example, our calculations using a smaller, 14-atom cell of LiMn_2O_4 , which also relaxes to a tetragonal structure but with a different $\text{Mn}^{3+}/\text{Mn}^{4+}$ ar-

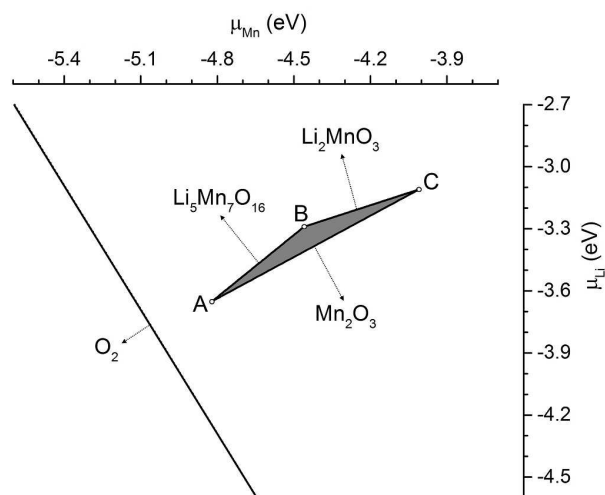


Fig. 3 Chemical-potential diagram at 0 K for LiMn_2O_4 . Only the O_2 gas phase and the Li–Mn–O phases that define the stability region, here shown as a shaded triangle, are included.

range, give band gaps of 1.77 and 1.92 eV for the FM and AFM configurations.

Experimentally, Raja *et al.*⁵³ reported an optical band gap of 1.43 eV from ultraviolet-visible spectroscopy for nanocrystalline LiMn_2O_4 powders with a nominal composition of $\text{Li}_{0.88}\text{Mn}_2\text{O}_4$. Kushida and Kuriyama,⁵⁴ on the other hand, observed two optical absorption peaks associated with d–d transitions at about 1.63 and 2.00 eV in LiMn_2O_4 thin films on silica glass. The discrepancies in the experimental values suggest that the band gap value is sensitive to the quality of the LiMn_2O_4 samples, which in turn depends on the synthesis conditions. This obviously complicates the comparison between the calculated and measured bulk properties.

3.2 Chemical-potential diagram

Figure 3 shows the atomic chemical-potential diagram for LiMn_2O_4 , constructed by exploring all possible Li–Mn–O phases available in the Materials Project database.⁵⁵ The stability region of LiMn_2O_4 in the $(\mu_{\text{Li}}, \mu_{\text{Mn}})$ plane is defined by Mn_2O_3 , Li_2MnO_3 , and $\text{Li}_5\text{Mn}_7\text{O}_{16}$. The calculated formation enthalpies at 0 K of tetragonal LiMn_2O_4 , orthorhombic Mn_2O_3 , monoclinic Li_2MnO_3 , and orthorhombic $\text{Li}_5\text{Mn}_7\text{O}_{16}$ are, respectively, -13.89 eV, -10.09 eV, -12.30 eV, and -54.39 eV/f.u. For comparison, the experimental formation enthalpy of LiMn_2O_4 at 298 K is -14.31 eV/f.u.⁵⁶ Points A, B, and C represent three-phase equilibria associated with LiMn_2O_4 . Point A, for example, is an equilibrium between LiMn_2O_4 , Mn_2O_3 , and $\text{Li}_5\text{Mn}_7\text{O}_{16}$. The presence of these equilibria is consistent with the fact that LiMn_2O_4

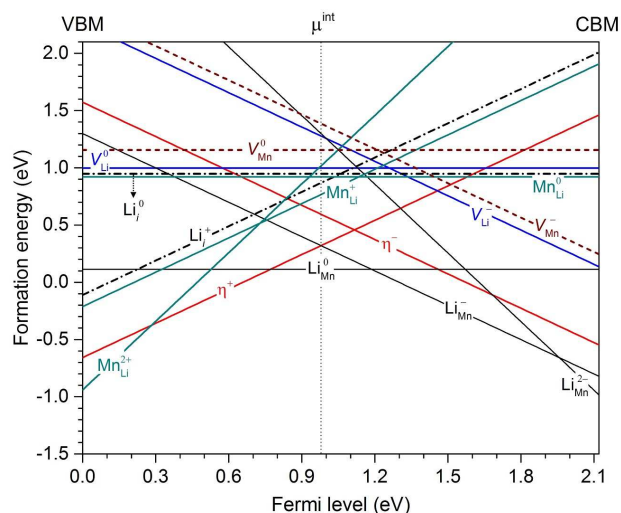


Fig. 4 Calculated formation energies of intrinsic point defects in LiMn_2O_4 , plotted as a function of the Fermi level. The energies are obtained at point B in Fig. 3. In the absence of extrinsic charged impurities, the Fermi level is at $\mu_e = \mu_e^{\text{int}}$, where charge neutrality is maintained.

samples often contain Mn_2O_3 and/or Li_2MnO_3 as impurity phases.^{17,57,58} Strobel *et al.*¹² also reported that annealing LiMn_2O_4 under oxygen pressures in the range 0.2–5 atm at 450°C resulted in Mn atoms being expelled in form of Mn_2O_3 . $\text{Li}_5\text{Mn}_7\text{O}_{16}$, which can be rewritten as $\text{Li}_{1+\alpha}\text{Mn}_{2-\alpha}\text{O}_4$ ($\alpha = 0.25$), is also closely related to LiMn_2O_4 . In fact, in the Li–Mn–O phase diagram, it is located on the tie-line between LiMn_2O_4 ($\alpha = 0$) where the average Mn oxidation state is +3.5 and $\text{Li}_4\text{Mn}_5\text{O}_{12}$ ($\alpha = 0.33$) where all Mn ions have the oxidation state of +4.

3.3 Defect structure and energetics

Figure 4 shows the calculated formation energies of low-energy defects in LiMn_2O_4 , obtained at point B in the chemical-potential diagram. These defects include hole (η^+) and electron (η^-) polarons, lithium vacancies (V_{Li}), interstitials (Li_i), and antisites (Li_{Mn}), and manganese vacancies (V_{Mn}) and antisites (Mn_{Li}). The formation energies are plotted as a function of the Fermi level μ_e , with μ_e varies from the VBM to CBM. As mentioned earlier, the actual position of the Fermi level of the system is determined by the charge neutrality condition. In the absence of electrically active impurities that can shift the Fermi-level position or when such impurities occur in much lower concentrations than charged intrinsic defects, the Fermi level is at μ_e^{int} , determined only by the intrinsic defects.^{33,34} With the chosen set of the atomic chemical potentials, μ_e^{int} is at 0.98 eV, exclusively defined by small hole polarons (η^+) and negatively charged lithium antisites (Li_{Mn}^-).

We find that intrinsic point defects in LiMn_2O_4 have very low formation energies and hence can occur with high concentrations. Polarons and charged lithium and manganese antisites have positive calculated formation energies only near midgap. Positively charged lithium interstitials (Li_i^+) also have a negative formation energy near the VBM. Before discussing the implications of these results, let us describe the defects in more detail.

Small polarons. A hole (or electron) polaron is a quasiparticle formed by the hole (electron) and its self-induced local lattice distortion. The creation of η^+ involves removing an electron from the VBM which is predominantly Mn^{3+} 3d states. This results in a Mn^{4+} ion at one of the Mn^{3+} sites, *i.e.*, a localized hole. The local lattice geometry near the newly formed Mn^{4+} ion is slightly distorted with the six neighboring O atoms moving toward the Mn^{4+} . The average Mn–O bond length at the Mn^{4+} site is 1.92 Å and the Jahn-Teller distortion vanishes at this site. The formation of η^- , on the other hand, corresponds to adding an electron to the CBM, which is predominantly Mn^{4+} 3d states, resulting in a Mn^{3+} ion at one of the Mn^{4+} sites, *i.e.*, a localized electron. The local geometry near the newly formed Mn^{3+} ion is also distorted, but with the neighboring O atoms slightly moving away from Mn^{3+} . At this Mn^{3+} site, there are four short and two long Mn–O bonds with the average bond lengths of 1.93 and 2.17 Å, respectively. Since the distortion is limited mainly to the neighboring O atoms of the resulted Mn^{3+} or Mn^{4+} ion, these polarons can be regarded as small polarons.⁵⁹

We find that the calculated formation energy of the polarons is as low as 0.32 eV (η^+) or 0.47 eV (η^-), in which η^+ is always energetically more favorable. It should be noted that these are additionally formed polarons, *i.e.*, they are considered as “defects” as compared to the perfect bulk material. The self-trapping energies of η^+ and η^- are 0.82 and 1.02 eV, respectively, defined as the difference between the formation energy of the free hole or electron and that of the hole or electron polaron.³⁴ With these high self-trapping energies, the polarons are very stable in LiMn_2O_4 . This is not surprising, given the consideration that half of the Mn sites in the host compound can be regarded as being stable as hole polarons (Mn^{4+}) in a hypothetical all- Mn^{3+} LiMn_2O_4 and the other half can be regarded as electron polarons (Mn^{3+}) in a hypothetical all- Mn^{4+} LiMn_2O_4 .

Vacancies and interstitials. The formation of V_{Li}^- involves removing a Li^+ ion, which causes negligible disturbance in the lattice. V_{Li}^0 is, on the other hand, created by removing a Li atom, which is in fact a Li^+ ion and an electron from a neighboring Mn atom. This results in a void at the site of the removed Li^+ and a Mn^{4+} at a neighboring Mn site (originally a Mn^{3+} ion). V_{Li}^0 is thus not the neutral charge state of a lithium vacancy but a complex of V_{Li}^- and η^+ . This defect complex has a binding energy of 0.60 eV with respect to V_{Li}^-

and η^+ . Defects such as V_{Li}^- , as well as η^+ and η^- , are regarded as *elementary* defects; the structure and energetics of other defects, *e.g.*, V_{Li}^0 , can be interpreted in terms of these basic building blocks. We find that the formation energy of V_{Li}^0 is always lower than that of V_{Li}^- . For lithium interstitials, Li_i^+ is created by adding a Li^+ ion. The defect is energetically most favorable when combining with another Li^+ ion from an 8a site to form a Li–Li dumbbell centered at the 8a site. This is in contrast to what has been commonly assumed that lithium interstitials are most stable at the 16c sites. The energy in the dumbbell configuration is lower than that at the 16c site by at least 0.15 eV. Finally, Li^0 , created by adding a Li atom, is a complex of Li^+ and η^- with a binding energy of 0.52 eV.

Among the manganese vacancies, V_{Mn}^{3-} , *i.e.*, the removal of a Mn^{3+} ion, is the elementary defect. Other defects such as V_{Mn}^{2-} , V_{Mn}^- , or V_{Mn}^0 are complexes of V_{Mn}^{3-} and, respectively, one, two, or three η^+ . V_{Mn}^0 is found to be the lowest-energy manganese vacancy configuration, suggesting that it is more favorable to form a manganese vacancy when it is surrounded by Mn^{4+} ions. The removal of manganese from the Mn^{3+} site costs less energy than from the Mn^{4+} site; the formation energy difference is about 0.20 eV or higher. Regarding the oxygen vacancies, the removal of an O^{2-} ion does not lead to a void formed by the removed ion, often denoted as V_{O}^{2+} , but a complex of V_{O}^{2+} and a hole-electron polaron pair ($\eta^+ - \eta^-$), hereafter denoted as V_{Ox}^{2+} . Clearly, V_{O}^{2+} is not stable as a single point defect, and its formation is associated with some $\text{Mn}^{3+}/\text{Mn}^{4+}$ disorder. Other oxygen vacancies such as V_{O}^+ or V_{O}^0 are complexes of V_{O}^{2+} and one or two η^- . We find that the oxygen vacancies have much higher formation energies than other intrinsic defects; their lowest value is 1.49 eV for V_{O}^0 at point C in the chemical-potential diagram. We also investigated manganese and oxygen interstitials and found that they all have very high formation energies (about 3 eV or higher), suggesting that these interstitials are not likely to form in the material.

Antisite defects. Lithium antisites Li_{Mn} are created by replacing Mn at a Mn site with Li. $\text{Li}_{\text{Mn}}^{2-}$, *i.e.*, Li^+ substituting Mn^{3+} , is an elementary defect. Other antisites such as Li_{Mn}^- or Li_{Mn}^0 are complexes of $\text{Li}_{\text{Mn}}^{2-}$ and, respectively, one or two η^+ . Among all possible ionic defects in LiMn_2O_4 , Li_{Mn}^0 has the lowest formation energy, as low as 0.11 eV. Figure 5 shows the structure of Li_{Mn}^0 where $\text{Li}_{\text{Mn}}^{2-}$ is clearly seen surrounded by six Mn^{4+} ions (*i.e.*, η^+) and six Li^+ ions. It should be noted that the two η^+ in the Li_{Mn}^0 complex are created together with the $\text{Li}_{\text{Mn}}^{2-}$, in addition to those Mn^{4+} ions already present in bulk LiMn_2O_4 . We find that the energy cost for ion substitution at the Mn^{3+} site is lower than at the Mn^{4+} site; the energy difference is 0.26 eV or higher. Manganese antisites Mn_{Li} are created in a similar way by replacing Li at a Li (tetrahedral) site with Mn. Mn_{Li}^+ is an elementary defect, in which the Mn

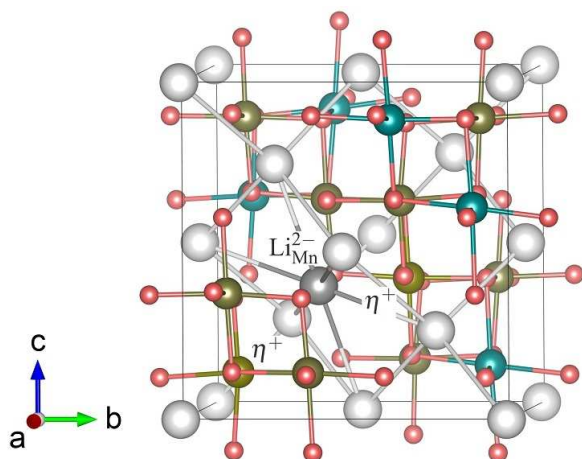


Fig. 5 Structure of Li_{Mn}^0 , the intrinsic ionic defect with the lowest formation energy in LiMn_2O_4 . This neutral defect is a complex of one negatively charged antisite $\text{Li}_{\text{Mn}}^{2-}$ (large dark gray sphere) and two small hole polarons η^+ (medium light yellow spheres).

ion is stable as high-spin Mn^{2+} with a calculated magnetic moment of $4.45 \mu_{\text{B}}$. Other manganese antisites such as Mn_{Li}^0 or $\text{Mn}_{\text{Li}}^{2+}$ are complexes of Mn_{Li}^+ and η^- or η^+ . For comparison, in layered LiMO_2 ($\text{M} = \text{Ni}, \text{Co}$) the transition metal is also found to be stable as high-spin M^{2+} at the Li (octahedral) site.³⁴

Defect complexes. In addition to the above defects, we explicitly investigated hole–electron polaron pairs ($\eta^+ - \eta^-$), antisite defect pairs ($\text{Mn}_{\text{Li}} - \text{Li}_{\text{Mn}}$), and lithium Frenkel pair ($\text{Li}_{\text{Li}}^+ - \text{V}_{\text{Li}}^-$). The hole–electron polaron pair is formed by switching the positions of a Mn^{3+} and its neighboring Mn^{4+} ion. After structural relaxations, the pair distance is 2.93 \AA . This defect pair has a formation energy of 0.37 eV and a binding of 0.54 eV . The antisite pair is created by switching the positions of a Li atom and its neighboring Mn atom. This ultimately results in a $\text{Mn}_{\text{Li}}^+ - \text{Li}_{\text{Mn}}^{2-} - \eta^+$ complex, in which the distance from the manganese antisite to the lithium antisite is 2.92 \AA and that from the lithium antisite to the hole polaron is 3.47 \AA . This complex has a formation energy of 0.63 eV and a binding of 1.76 eV . Finally, the lithium Frenkel pair is created by moving a Li^+ ion away from an 8a site to form a Li–Li dumbbell with another Li^+ ion. This results in a V_{Li}^- at the 8a site and a Li_{Li}^+ . After relaxations, the distance between the vacancy and the center of the dumbbell is about 4.0 \AA (The pair is unstable toward recombination at shorter distances). This pair has a formation energy of 1.85 eV and a binding energy of 0.30 eV . It should be noted that the formation energies of these three defect complexes are independent of the chemical potentials.

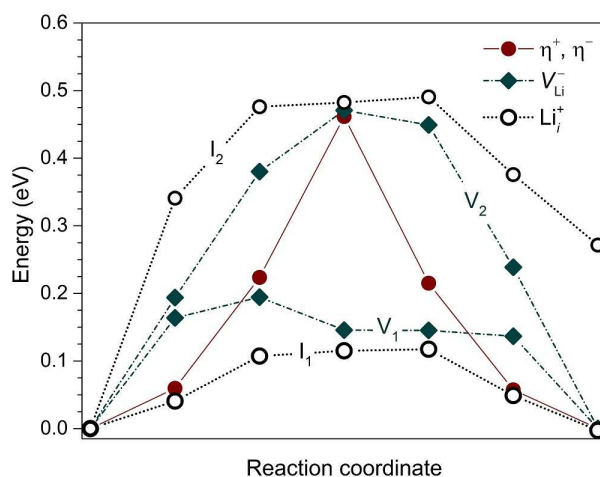


Fig. 6 Migration barriers of the small hole (η^+) and electron (η^-) polarons and lithium vacancies (V_{Li}^-) and interstitials (Li_{Li}^+) in long-range charge-ordered LiMn_2O_4 .

3.4 Defect migration

Figure 6 shows the migration barriers (E_m) for the hole and electron polarons and lithium vacancies and interstitials in LiMn_2O_4 . All the migration barrier calculations were carried out with the Γ point only. The migration of a polaron between two positions \mathbf{q}_1 and \mathbf{q}_2 can be described by the transfer of the lattice distortion over a one-dimensional Born-Oppenheimer surface.⁶⁰ We estimate the energy barrier by computing the energies of a set of cell configurations linearly interpolated between \mathbf{q}_1 and \mathbf{q}_2 and identify the energy maximum. The migration barrier of η^+ and η^- is found to be 0.46 eV . For comparison, Ouyang *et al.*²⁷ reported a migration barrier of 0.35 eV for polarons in LiMn_2O_4 , obtained in GGA+ U calculations with $U = 4.5 \text{ eV}$.

For lithium vacancies V_{Li}^- , we find two distinct migration paths with barriers of 0.19 eV (path V_1) and 0.47 eV (path V_2), calculated using the NEB method.⁴⁷ Both paths involve moving a Li^+ ion from an 8a site to the vacancy (an empty 8a site) through an interstitial 16c site. Here, moving a Li^+ ion in one direction is equivalent to V_{Li}^- migrating in the opposite direction. The migration bottleneck is a Mn ring at the 16c site, consisting of six Mn ions in the plane perpendicular to the migration path. In path V_1 , the Mn ring has four Mn^{4+} ions and two Mn^{3+} ions, whereas in path V_2 it has two Mn^{4+} ions and four Mn^{3+} ions. We have also considered situations in which Li^+ ions migrate through a Mn ring that consists of three Mn^{4+} ions and three Mn^{3+} ions and find migration barriers of $0.47 - 0.57 \text{ eV}$. An example of such situations is when the η^+ component of the V_{Li}^0 complex is kept fixed while the V_{Li}^- component of the complex is migrating.

Lithium interstitials Li_{Li}^+ migrate through an interstitialcy

mechanism involving concerted motion of three lithium ions: two ions of the Li–Li dumbbell and one ion that is next to the dumbbell. We find barriers of 0.12 eV for the migration path (hereafter called path I₁) that goes through Mn rings all consisting of four Mn⁴⁺ ions and two Mn³⁺ ions, and 0.49 eV for the path (path I₂) that goes through at least one Mn ring that consists of two Mn⁴⁺ ions and four Mn³⁺ ions.

For comparison, Xu and Meng²⁹ obtained from GGA+*U* calculations with *U* = 4.84 eV lithium migration barriers of ~0.2–0.4 eV associated with Mn⁴⁺-rich rings, ~0.6 eV with Mn³⁺-rich rings, and ~0.8 eV with Mn rings that have equal numbers of Mn⁴⁺ and Mn³⁺ ions. The migrating species in their calculations could be V_{Li}⁰, instead of V_{Li}⁻ like in our calculations. However, it is not clear from their work how the two components of the V_{Li}⁰ complex migrate relative to each other. We note that, in our calculations, a lower bound on the migration barrier of a defect complex, *e.g.*, V_{Li}⁰ or Li_i⁰, can be estimated by taking the higher of the migration barriers of its constituents.⁶¹

We find that the tetragonal distortion has minor effects on the migration barriers. For example, our calculations using cubic supercells that have the same volume and Mn³⁺/Mn⁴⁺ arrangement as the tetragonal supercells give V_{Li}⁻ barriers of 0.20 eV and 0.45 eV for paths V₁ and V₂, respectively, which are almost identical to the values reported earlier. However, in the presence of Mn³⁺/Mn⁴⁺ disorder and other lattice defects, *e.g.*, in lithium over-stoichiometric Li[Mn_{2-α}Li_α]O₄, the lithium ions are not likely to encounter Mn rings that are all Mn⁴⁺-rich for the whole diffusion length, and the overall migration barrier will therefore be determined by the higher-barrier segment. As a result, the hole and electron polarons and lithium vacancies and interstitials, except the lithium at the octahedral 16d site (see below), all have an estimated migration barrier of about 0.5 eV.

Finally, we investigated the migration of the Li⁺ ion that is associated with the lithium antisite Li_{Mn}⁰, *cf.* Fig. 5. The energy barrier for Li⁺ migration from the 16d site to one of the six neighboring Li sites through a vacancy mechanism is found to be 0.6–2.0 eV. With this higher migration barrier, the ion is trapped at the 16d site and expected not to be deintercalated during charging.

4 Discussion

We list in Table 1 the calculated formation energies of relevant point defects in LiMn₂O₄ for three different sets of the atomic chemical potentials, corresponding to different sets of the experimental conditions. The chemical potential of oxygen, μ_O, is -0.15 eV, -0.42 eV, and -0.69 eV, respectively, at points A, B, and C in the chemical-potential diagram, *cf.* Fig. 3. μ_O can be controlled by controlling temperature and pressure and/or oxygen reducing agents. Lower μ_O values are usually

Table 1 Formation energies (*E^f*) and binding energies (*E_b*) of intrinsic defects in LiMn₂O₄. The formation energies are obtained at points A, B, and C in the chemical-potential diagram

Defect	<i>E^f</i> (eV)			Constituents	<i>E_b</i> (eV)
	A	B	C		
η ⁺	0.32	0.32	0.45		
η ⁻	0.59	0.59	0.47		
η ⁺ –η ⁻	0.37	0.37	0.37	η ⁺ + η ⁻	0.54
V _{Li} ⁻	0.92	1.28	1.33		
V _{Li} ⁰	0.64	1.00	1.18	V _{Li} ⁻ + η ⁺	0.60
Li _i ⁺	1.23	0.87	0.82		
Li _i ⁰	1.30	0.94	0.76	Li _i ⁺ + η ⁻	0.52
Li _i ⁺ –V _{Li} ⁻	1.85	1.85	1.85	Li _i ⁺ + V _{Li} ⁻	0.30
Li _{Mn} ²⁻	1.30	1.30	1.31		
Li _{Mn} ⁻	0.32	0.32	0.46	Li _{Mn} ²⁻ + η ⁺	1.30
Li _{Mn} ⁰	0.11	0.11	0.38	Li _{Mn} ²⁻ + 2η ⁺	1.82
Mn _i ⁺	0.77	0.77	0.62		
Mn _{Li} ⁰	0.92	0.92	0.65	Mn _{Li} ⁺ + η ⁻	0.44
Mn _{Li} ²⁺	1.02	1.02	1.00	Mn _{Li} ⁺ + η ⁺	0.07
Mn _{Li} –Li _{Mn}	0.63	0.63	0.63	Mn _{Li} ⁺ + Li _{Mn} ²⁻ + η ⁺	1.76
V _{Mn} ³⁻	3.11	3.47	3.51		
V _{Mn} ²⁻	1.80	2.16	2.34	V _{Mn} ³⁻ + η ⁺	1.63
V _{Mn} ⁻	1.03	1.39	1.71	V _{Mn} ³⁻ + 2η ⁺	2.72
V _{Mn} ⁰	0.80	1.16	1.61	V _{Mn} ³⁻ + 3η ⁺	3.27
V _{O*} ²⁺	2.42	2.15	2.15	V _O ²⁺ + η ⁺ + η ⁻	
V _O ⁺	2.15	1.88	1.75	V _O ²⁺ + η ⁻	
V _O ⁰	2.03	1.76	1.49	V _O ²⁺ + 2η ⁻	

associated with higher temperatures and/or lower oxygen partial pressures and/or the presence of oxygen reducing agents. For each set of the chemical potentials, the formation energy values are obtained at the respective Fermi-level position μ_e^{int}. We find that μ_e^{int} is at 0.98–1.11 eV, which is always away from both the VBM and CBM. Most of the defects have a calculated formation energy of 1.0 eV or lower, at least under certain conditions. They can therefore occur in the material with high concentrations, *e.g.*, during synthesis. These defects, except the mobile ones such as the polarons and lithium vacancies, are expected to get trapped when the material is cooled to room temperature. We also find that the formation energy of the polaron pair η⁺–η⁻ is low, only 0.37 eV, indicating that LiMn₂O₄ is prone to Mn³⁺/Mn⁴⁺ disorder. Mn_{Li}–Li_{Mn} also has a low formation energy, which suggests the presence of cation mixing (see more in Sections 4.3 and 4.4).

4.1 Electronic and ionic conduction

Strictly speaking, each ionic defect in LiMn₂O₄ has only one stable charge state, which is also called the elementary defect; oxygen vacancies do not even have any configuration that is stable as a single point defect, as mentioned earlier.

Removing/adding electrons from/to these elementary defects always results in defect complexes consisting of the elementary defects and small hole/electron polarons. Besides, several positively and negatively charged defects have positive formation energies only near midgap, *cf.* Fig. 4, making them perfect charge-compensators. Any attempt to deliberately shift the Fermi level of the system from μ_e^{int} to the VBM or CBM will result in the charged defects having negative formation energies, *i.e.*, the intrinsic defects will form spontaneously and counteract the effects of shifting.^{33,34} Clearly, intrinsic point defects in LiMn_2O_4 cannot act as sources of band-like electrons and holes, and the material cannot be made n-type or p-type. The electronic conduction therefore proceeds via hopping of small hole and electron polarons. Regarding the ionic conduction, lithium ions are the current-carrying species, which migrate via vacancy and/or interstitial mechanisms.

The activation energies for electronic and ionic conduction can be estimated from the formation energies and migration barriers of the current-carrying defects, $E_a = E^f + E_m$. As discussed earlier, except for paths V_1 and I_1 which are unlikely to be realized in $\text{Mn}^{3+}/\text{Mn}^{4+}$ -disordered LiMn_2O_4 , the barriers for the polarons and lithium ions are basically identical, ~ 0.5 eV. Therefore, the relative contribution of a defect or migration mechanism to the total conductivity is determined exclusively by the defect's concentration. If the defect is predominantly *athermal*, as it is the case for hole and electron polarons in LiMn_2O_4 and lithium vacancies in Li-deficient or partially delithiated $\text{Li}_{1-x}\text{Mn}_2\text{O}_4$, the activation energy includes only the migration part, *i.e.*, $E_a = E_m$.³⁴ The electronic activation energy is thus ~ 0.5 eV, *i.e.*, the barrier for polarons. In partially delithiated $\text{Li}_{1-x}\text{Mn}_2\text{O}_4$, the ionic activation energy is also ~ 0.5 eV, *i.e.*, the barrier for lithium vacancies. In stoichiometric LiMn_2O_4 , however, lithium vacancies and/or interstitials have to be thermally activated; the ionic activation energy includes both the migration (~ 0.5 eV) and formation (*cf.* Table 1) parts, which is estimated to be as low as ~ 1.1 eV (1.3 eV) for the lithium vacancy (interstitialcy) mechanism. Clearly, the total conductivity is dominated by the electronic contribution.

Experimentally, Fang and Chung²⁴ reported activation energies of 0.43 eV and 0.38 eV for electronic conduction in LiMn_2O_4 below and above room temperature, respectively. Other authors reported values of 0.40–0.44 eV.^{22,23} Regarding lithium diffusion, Verhoeven *et al.*⁶² obtained an activation energy of 0.5 ± 0.1 eV in the temperature range 345–400 K from ^7Li NMR experiments on $\text{Li}[\text{Mn}_{1.96}\text{Li}_{0.04}]\text{O}_4$. Takai *et al.*⁶³ reported activation energies of 0.52 eV and 1.11 eV for lithium diffusion in LiMn_2O_4 below and above 600°C, extracted from tracer diffusion coefficients measured by neutron radiography. The lower-temperature values are very close to our estimated migration barrier. The value 1.11 eV at high temperatures could indicate that the system is in the intrinsic

region where the activation energy includes both the formation and migration parts.

4.2 Delithiation and lithiation

The structure of the lithium vacancy V_{Li}^0 in a battery electrode material often provides direct information on the delithiation mechanism. In LiMn_2O_4 , V_{Li}^0 indicates that for each Li atom removed from LiMn_2O_4 electrodes during delithiation, the material is left with one negatively charged lithium vacancy V_{Li}^- and one hole polaron η^+ ; *i.e.*, the extraction of Li is associated with the oxidation of Mn^{3+} to Mn^{4+} . The deintercalation voltage⁶⁴ associated with the extraction of the first lithium, *i.e.*, the creation of V_{Li}^0 , is 4.29 V. The partially delithiated composition can be written as $\text{Li}_{1-x}\text{Mn}_2\text{O}_4$ (Here we ignore the pre-existing intrinsic defects which will be discussed later). The lithium interstitial Li_i^0 , on the other hand, provides information on the lithiation mechanism. For each Li atom inserted into LiMn_2O_4 electrodes during lithiation, the material receives one positively charged lithium interstitial Li_i^+ and one electron polaron η^- ; *i.e.*, the Li insertion is associated with the reduction of Mn^{4+} to Mn^{3+} . The partially lithiated composition is $\text{Li}_{1+x}\text{Mn}_2\text{O}_4$ (Not to be confused with lithium overstoichiometric $\text{Li}_{1+\alpha}\text{Mn}_{2-\alpha}\text{O}_4$ where the Li excess replaces Mn at the 16d sites). Since there are no band-like carriers, η^+ and η^- are the electronic charge carriers in the delithiation and lithiation processes. Also, it is important to note that polarons and lithium vacancies/interstitials created from delithiation/lithiation are not thermal defects.

4.3 Lithium over-stoichiometry

Among all possible ionic defects in LiMn_2O_4 , the lithium antisite Li_{Mn}^0 is dominant. The defect has a formation energy of 0.11–0.38 eV, depending the specific set of the atomic chemical potentials. For comparison, the calculated formation energy of the lithium antisite in layered LiCoO_2 and LiNiO_2 is in the range of 0.92–2.73 eV (Li_{Co}^0) or 0.68–1.11 eV (Li_{Ni}^0).³⁴ The low energy of Li_{Mn}^0 can partially be ascribed to the small difference in the ionic radii of Li^+ (0.76 Å) and high-spin Mn^{3+} (0.65 Å); for reference, the Shannon ionic radii of six-fold coordinated, low-spin Co^{3+} and Ni^{3+} are 0.55 Å and 0.56 Å, respectively.⁶⁵ Given Li_{Mn}^0 with that low formation energy, the synthesis of LiMn_2O_4 under equilibrium or near-equilibrium conditions is expected to result in a lithium over-stoichiometric compound with the composition $\text{Li}_{1+\alpha}\text{Mn}_{2-\alpha}\text{O}_4$ or, explicitly, $\text{Li}[\text{Mn}_{2-\alpha}\text{Li}_\alpha]\text{O}_4$ or $\text{Li}^+[\text{Mn}_{1-3\alpha}^{3+}\text{Mn}_{1+2\alpha}^{4+}\text{Li}_\alpha^+]\text{O}_4^{2-}$. In this composition, each negatively charged lithium antisite $\text{Li}_{\text{Mn}}^{2-}$ is charge-compensated by two hole polarons η^+ , and the average Mn oxidation state is higher than +3.5; *i.e.*, Mn^{4+} is slightly more favorable than Mn^{3+} . Since the Li^+ ion at the octahedral 16d site gets trapped

due to its lower mobility, it is unlikely to be deintercalated during charging. Besides, $\text{Li}[\text{Mn}_{2-\alpha}\text{Li}_\alpha]\text{O}_4$ has only $(1-3\alpha)$ Mn^{3+} ions for the oxidation reactions. As a result, there will be residual lithium in the fully delithiated compound, both at the 16d and 8a sites, *i.e.*, $\text{Li}_{3\alpha}^+[\text{Mn}_{2-\alpha}^{4+}\text{Li}_\alpha^+]\text{O}_4^{2-}$. The theoretical capacity of LiMn_2O_4 will therefore decrease from 148 mAh/g to $148(1-3\alpha)$ mAh/g.

Our results for Li_{Mn}^0 thus explain why LiMn_2O_4 samples are often lithium over-stoichiometric. Martinez *et al.*¹³ found about 90% of the lithium ions at the tetrahedral 8a sites and 10% at the octahedral 16d sites, confirming that the Li excess replaces Mn at the 16d sites. Xia and Yoshio²¹ seemed to indicate that stoichiometric LiMn_2O_4 electrodes are unstable toward the lithium over-stoichiometric ones. We note that, as a consequence of the lithium over-stoichiometry and the likely random distribution of Li_{Mn}^0 , the transformation from the $\text{Mn}^{3+}/\text{Mn}^{4+}$ -disordered, cubic phase to a long-range ordered, tetragonal/orthorhombic phase may not be realized in practice, even at low temperatures. In fact, there have been reports of the absence of the long-range charge order associated with the Jahn-Teller effect in lithium over-stoichiometric $\text{Li}_{1+\alpha}\text{Mn}_{2-\alpha}\text{O}_4$.^{15,19} Kamazawa *et al.*,¹⁹ for example, observed only short-range charged-order in $\text{Li}_{1.1}\text{Mn}_{1.9}\text{O}_4$. Regarding the electrochemical performance, $\text{Li}_{1+\alpha}\text{Mn}_{2-\alpha}\text{O}_4$ samples have been reported to show a significantly enhanced cycling stability compared to stoichiometric LiMn_2O_4 , although at the expense of capacity.^{20,21} The enhancement has been attributed mainly to the suppression of the Jahn-Teller effect on deep discharge. However, the presence of the residual lithium in the delithiated compound, *i.e.*, $\text{Li}_{3\alpha}^+[\text{Mn}_{2-\alpha}^{4+}\text{Li}_\alpha^+]\text{O}_4^{2-}$, can also help improve the cycling stability, unlike in LiMn_2O_4 where the complete extraction of lithium results in unstable λ - MnO_2 electrodes.²⁰

4.4 Other possible defects

The manganese antisite Mn_{Li}^+ can occur in LiMn_2O_4 , given its formation energy of only 0.62–0.77 eV. For comparison, the formation energy of Co_{Li}^+ in LiCoO_2 is 0.55–2.08 eV and that of Ni_{Li}^+ in LiNiO_2 is 0.53–0.96 eV.³⁴ Mn_{Li}^+ can be created together with $\text{Li}_{\text{Mn}}^{2-}$ and η^+ , *i.e.*, in form of $\text{Mn}_{\text{Li}}-\text{Li}_{\text{Mn}}$ with a formation energy of 0.63 eV, or with η^- , *i.e.*, in form of Mn_{Li}^0 with a formation energy of 0.65–0.92 eV, *cf.* Table 1. Manganese antisites have also been observed in experiments. Björk *et al.*¹¹ reported that 9% of the lithium ions at the tetrahedral 8a sites were substituted by Mn^{2+} ions in high-temperature synthesis. This is consistent with our results showing that Mn_{Li}^+ has the lowest formation energy at point C which corresponds to a low μ_{O} value. If created in form of Mn_{Li}^0 , the co-generation of η^- will result in an increase in the amount of the Jahn-Teller distorted Mn^{3+} ions. Besides, we speculate that manganese antisites may also act as nucleation

sites for the formation of impurity phases during electrochemical cycling.

Next, with a formation energy of 0.76–1.23 eV, lithium interstitials can also occur in the material, *e.g.*, when synthesized under conditions near point C in the chemical-potential diagram, *cf.* Fig. 3. Li_i^+ can be created together with η^- , *i.e.*, in form of Li_i^0 which results in the composition $\text{Li}_{1+\alpha}\text{Mn}_2\text{O}_4$ (assuming no other defects). In this composition, the average Mn oxidation state is <3.5 . This defect is unlikely to form through the lithium Frenkel pair mechanism, *i.e.*, in combination with V_{Li}^- , because the $\text{Li}_i^+-V_{\text{Li}}^-$ pair is either unstable or high in energy. Experimentally, Berg *et al.*¹⁷ reported that, in their $\text{Li}_{1+\alpha}\text{Mn}_{2-\alpha}\text{O}_4$ ($\alpha = 0.14$) samples, lithium ions occupy both the 8a sites with 100% occupancy and the 16c sites with 7.0% occupancy, and manganese ions occupy the 16d sites with 93.0% occupancy. In light of our results for the lithium interstitials, it would be interesting to re-examine the samples and see if some of the lithium is really stable at the 16c sites. The results of Berg *et al.* may also suggest the presence of Li_i and V_{Mn} in form of a neutral $\text{Li}_i-V_{\text{Mn}}$ complex. However, we find that this complex has a high formation energy (1.93–2.20 eV), indicating that it is not likely to occur under equilibrium or near-equilibrium synthesis conditions.

Manganese vacancies can form when synthesized at lower temperatures, *e.g.*, at point A in Fig. 3 where the formation energy of V_{Mn}^0 is just 0.80 eV, *cf.* Table 1. Gummow *et al.*²⁰ reported the presence of vacancies on both the 8a and 16d sites in $\text{Li}_{1-\alpha}\text{Mn}_{2-2\alpha}\text{O}_4$ ($0 < \alpha \leq 0.11$) synthesized at temperatures between 400 and 600°C, although they also acknowledged that samples with a precise, predetermined composition were difficult to prepare. The cycling stability of this compound was found to be inferior to that of $\text{Li}_{1+\alpha}\text{Mn}_{2-\alpha}\text{O}_4$.²⁰ Finally, with a much higher formation energy (1.49–2.03 eV), oxygen vacancies are expected not to occur inside the material. This is consistent with experiments where no oxygen vacancies have been found.^{11,14} We note that oxygen vacancies may still occur at the surface or interface where the lattice environment is less constrained than in the bulk. The formation of manganese vacancies, as well as lithium interstitials and manganese antisites, is also expected to be more favorable at the surface/interface than in the bulk.

Apparently, manganese antisites and vacancies and lithium interstitials can lead to inferior cycling stability and hence should be avoided. One can tune the synthesis conditions to reduce these defects in LiMn_2O_4 samples. From our results summarized in Table 1, the best compromise could be to synthesize the material under the conditions near point B in the chemical-potential diagram where there is a three-phase equilibrium between LiMn_2O_4 , Li_2MnO_3 and $\text{Li}_5\text{Mn}_7\text{O}_{16}$, *cf.* Fig. 3. The formation energy of the manganese antisites under these conditions is, however, still quite low (0.77 eV). Further reduction of the defects may thus require partially ion

substitution that can significantly change the chemical environment and hence the defect landscape.

5 Conclusions

We have carried out a DFT study of the bulk properties and defect thermodynamics and transport in spinel-type LiMn_2O_4 , using the HSE06 screened hybrid density functional. We find that the tetragonal distortion of cubic LiMn_2O_4 during structural optimizations at 0 K is associated with charge ordering. The compound is found to be thermodynamically stable and its stability region in the Li–Mn–O phase diagram is defined by the Mn_2O_3 , Li_2MnO_3 , and $\text{Li}_5\text{Mn}_7\text{O}_{16}$ phases.

Intrinsic electronic and ionic defects in LiMn_2O_4 can form with high concentrations. Several charged defects have positive formation energies only in a region near midgap, making them perfect charge-compensators. The defects cannot act as sources of band-like carriers and the material cannot be doped n- or p-type. The electronic conduction proceeds via hopping of the small hole and electrons polarons and the ionic conduction occurs via lithium vacancy and/or interstitial migration mechanisms. The total bulk conductivity is predominantly from the electronic contribution. A analysis of the structure of lithium vacancies and interstitials shows that lithium extraction (insertion) is associated with the oxidation (reduction) reaction at the Mn site.

Among the intrinsic ionic defects, lithium antisites are the dominant defect with a very low formation energy. This low energy is ascribed to the small ionic radius difference between Li^+ and high-spin Mn^{3+} . The formation energy of the hole-electron polaron pair is also very low. Our results thus indicate that LiMn_2O_4 is prone to lithium over-stoichiometry and $\text{Mn}^{3+}/\text{Mn}^{4+}$ disorder. In the lithium over-stoichiometric compound, there is residual lithium that is not deintercalated during charging and can help improve the cycling stability. Other defects such as manganese antisites and vacancies and lithium interstitials can also occur, under certain synthesis conditions, but with lower concentrations than the lithium antisites. An elimination of the manganese antisites may require significant changes to the chemical environment, *e.g.*, through ion substitution.

Acknowledgements

This work was supported by the U.S. Department of Energy (Grant No. DE-SC0001717) and the Center for Computationally Assisted Science and Technology at North Dakota State University.

References

1 Thackeray, M. M. *J. Am. Ceram. Soc.* **1999**, *82*, 3347–3354.

- 2 Park, O. K.; Cho, Y.; Lee, S.; Yoo, H.-C.; Song, H.-K.; Cho, J. *Energy Environ. Sci.* **2011**, *4*, 1621–1633.
- 3 Rodríguez-Carvajal, J.; Rousse, G.; Masquelier, C.; Hervieu, M. *Phys. Rev. Lett.* **1998**, *81*, 4660–4663.
- 4 Piszora, P.; Darul, J.; Nowicki, W.; Wolska, E. *J. Alloys Compd.* **2004**, *362*, 231–235.
- 5 Oikawa, K.; Kamiyama, T.; Izumi, F.; Chakoumakos, B. C.; Ikuta, H.; Wakihara, M.; Li, J.; Matsui, Y. *Solid State Ionics* **1998**, *109*, 35–41.
- 6 Akimoto, J.; Takahashi, Y.; Kijima, N.; Gotoh, Y. *Solid State Ionics* **2004**, *172*, 491–494.
- 7 Wills, A. S.; Raju, N. P.; Greedan, J. E. *Chem. Mater.* **1999**, *11*, 1510–1518.
- 8 Yamada, A.; Tanaka, M. *Mater. Res. Bull.* **1995**, *30*, 715–721.
- 9 Yonemura, M.; Kamiyama, T.; Kawamoto, Y.; Kanno, R. *Mater. Trans.* **2004**, *45*, 2048–2055.
- 10 Tarascon, J. M.; McKinnon, W. R.; Coowar, F.; Bowmer, T. N.; Amattucci, G.; Guyomard, D. *J. Electrochem. Soc.* **1994**, *141*, 1421–1431.
- 11 Björk, H.; Dabkowska, H.; Greedan, J. E.; Gustafsson, T.; Thomas, J. O. *Acta Crystallogr., Sect. C: Cryst. Struct. Commun.* **2001**, *57*, 331–332.
- 12 Strobel, P.; Rousse, G.; Ibarra-Palos, A.; Masquelier, C. *J. Solid State Chem.* **2004**, *177*, 1–5.
- 13 Martinez, S.; Sobrados, I.; Tonti, D.; Amarilla, J. M.; Sanz, J. *Phys. Chem. Chem. Phys.* **2014**, *16*, 3282–3291.
- 14 Paulsen, J. M.; Dahn, J. R. *Chem. Mater.* **1999**, *11*, 3065–3079.
- 15 Lee, Y. J.; Grey, C. P. *J. Electrochem. Soc.* **2002**, *149*, A103–A114.
- 16 Takada, T.; Hayakawa, H.; Enoki, H.; Akiba, E.; Slegre, H.; Davidson, I.; Murray, J. *J. Power Sources* **1999**, *81–82*, 505–509.
- 17 Berg, H.; M. Kelder, E.; O. Thomas, J. *J. Mater. Chem.* **1999**, *9*, 427–429.
- 18 Sugiyama, J.; Mukai, K.; Ikeda, Y.; Russo, P. L.; Suzuki, T.; Watanabe, I.; Brewer, J. H.; Ansaldo, E. J.; Chow, K. H.; Ariyoshi, K.; Ohzuku, T. *Phys. Rev. B* **2007**, *75*, 174424.
- 19 Kamazawa, K.; Nozaki, H.; Harada, M.; Mukai, K.; Ikeda, Y.; Iida, K.; Sato, T. J.; Qiu, Y.; Tyagi, M.; Sugiyama, J. *Phys. Rev. B* **2011**, *83*, 094401.
- 20 Gummow, R.; de Kock, A.; Thackeray, M. *Solid State Ionics* **1994**, *69*, 59–67.
- 21 Xia, Y.; Yoshio, M. *J. Electrochem. Soc.* **1996**, *143*, 825–833.
- 22 Massarotti, V.; Capsoni, D.; Bini, M.; Chiodelli, G.; Azzoni, C.; Mozzi, M.; Paleari, A. *J. Solid State Chem.* **1999**, *147*, 509–515.
- 23 Iguchi, E.; Tokuda, Y.; Nakatsugawa, H.; Munakata, F. *J. Appl. Phys.* **2002**, *91*, 2149–2154.
- 24 Fang, T.-T.; Chung, H.-Y. *J. Am. Ceram. Soc.* **2008**, *91*, 342–345.
- 25 Grechnev, G. E.; Ahuja, R.; Johansson, B.; Eriksson, O. *Phys. Rev. B* **2002**, *65*, 174408.
- 26 Wang, L.; Maxisch, T.; Ceder, G. *Chem. Mater.* **2007**, *19*, 543–552.
- 27 Ouyang, C.; Du, Y.; Shi, S.; Lei, M. *Physics Letters A* **2009**, *373*, 2796–2799.
- 28 Nakayama, M.; Nogami, M. *Solid State Commun.* **2010**, *150*, 1329–1333.
- 29 Xu, B.; Meng, S. *J. Power Sources* **2010**, *195*, 4971–4976.
- 30 Ammundsen, B.; Rozire, J.; Islam, M. S. *J. Phys. Chem. B* **1997**, *101*, 8156–8163.
- 31 Koyama, Y.; Tanaka, I.; Adachi, H.; Uchimoto, Y.; Wakihara, M. *J. Electrochem. Soc.* **2003**, *150*, A63–A67.
- 32 Perdew, J. P.; Zunger, A. *Phys. Rev. B* **1981**, *23*, 5048–5079.
- 33 Hoang, K.; Johannes, M. *Chem. Mater.* **2011**, *23*, 3003–3013.
- 34 Hoang, K.; Johannes, M. D. *J. Mater. Chem. A* **2014**, *2*, 5224–5235.
- 35 Perdew, J. P.; Burke, K.; Ernzerhof, M. *Phys. Rev. Lett.* **1996**, *77*, 3865–3868.
- 36 Mishra, S. K.; Ceder, G. *Phys. Rev. B* **1999**, *59*, 6120–6130.
- 37 Dudarev, S. L.; Botton, G. A.; Savrasov, S. Y.; Humphreys, C. J.; Sutton, A. P. *Phys. Rev. B* **1998**, *57*, 1505–1509.

- 38 Liechtenstein, A. I.; Anisimov, V. I.; Zaanen, J. *Phys. Rev. B* **1995**, *52*, R5467–R5470.
- 39 Heyd, J.; Scuseria, G. E.; Ernzerhof, M. *J. Chem. Phys.* **2003**, *118*, 8207–8215.
- 40 Paier, J.; Marsman, M.; Hummer, K.; Kresse, G.; Gerber, I. C.; Ángyán, J. G. *J. Chem. Phys.* **2006**, *124*, 154709.
- 41 Blöchl, P. E. *Phys. Rev. B* **1994**, *50*, 17953–17979.
- 42 Kresse, G.; Joubert, D. *Phys. Rev. B* **1999**, *59*, 1758–1775.
- 43 Kresse, G.; Hafner, J. *Phys. Rev. B* **1993**, *47*, 558–561.
- 44 Kresse, G.; Furthmüller, J. *Phys. Rev. B* **1996**, *54*, 11169–11186.
- 45 Kresse, G.; Furthmüller, J. *Comput. Mat. Sci.* **1996**, *6*, 15–50.
- 46 Monkhorst, H. J.; Pack, J. D. *Phys. Rev. B* **1976**, *13*, 5188–5192.
- 47 Henkelman, G.; Uberuaga, B. P.; Jónsson, H. *J. Chem. Phys.* **2000**, *113*, 9901–9904.
- 48 Van de Walle, C. G.; Neugebauer, J. *J. Appl. Phys.* **2004**, *95*, 3851–3879.
- 49 Freysoldt, C.; Neugebauer, J.; Van de Walle, C. G. *Phys. Rev. Lett.* **2009**, *102*, 016402.
- 50 Freysoldt, C.; Neugebauer, J.; Van de Walle, C. G. *phys. status solidi (b)* **2011**, *248*, 1067–1076.
- 51 Zhou, F.; Cococcioni, M.; Marianetti, C.; Morgan, D.; Ceder, G. *Phys. Rev. B* **2004**, *70*, 235121.
- 52 Mukai, K.; Sugiyama, J.; Kamazawa, K.; Ikedo, Y.; Andreica, D.; Amato, A. *J. Solid State Chem.* **2011**, *184*, 1096–1104.
- 53 Raja, M.; Mahanty, S.; Ghosh, P.; Basu, R.; Maiti, H. *Mater. Res. Bull.* **2007**, *42*, 1499–1506.
- 54 Kushida, K.; Kuriyama, K. *Appl. Phys. Lett.* **2000**, *77*, 4154–4156.
- 55 Jain, A.; Ong, S. P.; Hautier, G.; Chen, W.; Richards, W. D.; Dacek, S.; Cholia, S.; Gunter, D.; Skinner, D.; Ceder, G.; Persson, K. A. *APL Materials* **2013**, *1*, 011002.
- 56 Wang, M.; Navrotsky, A. *J. Solid State Chem.* **2005**, *178*, 1182–1189.
- 57 Gao, Y.; Dahn, J. R. *J. Electrochem. Soc.* **1996**, *143*, 100–114.
- 58 Luo, C.; Martin, M. *J. Mater. Sci.* **2007**, *42*, 1955–1964.
- 59 Stoneham, A. M.; Gavartin, J.; Shluger, A. L.; Kimmel, A. V.; Muñoz Ramo, D.; Rønnow, H. M.; Aepli, G.; Renner, C. *J. Phys.: Condens. Matter* **2007**, *19*, 255208.
- 60 Maxisch, T.; Zhou, F.; Ceder, G. *Phys. Rev. B* **2006**, *73*, 104301.
- 61 Wilson-Short, G. B.; Janotti, A.; Hoang, K.; Peles, A.; Van de Walle, C. G. *Phys. Rev. B* **2009**, *80*, 224102.
- 62 Verhoeven, V. W. J.; de Schepper, I. M.; Nachtegaal, G.; Kentgens, A. P. M.; Kelder, E. M.; Schoonman, J.; Mulder, F. M. *Phys. Rev. Lett.* **2001**, *86*, 4314–4317.
- 63 Takai, S.; Yoshioka, K.; Iikura, H.; Matsubayashi, M.; Yao, T.; Esaka, T. *Solid State Ionics* **2014**, *256*, 93–96.
- 64 Aydinol, M. K.; Kohan, A. F.; Ceder, G.; Cho, K.; Joannopoulos, J. *Phys. Rev. B* **1997**, *56*, 1354–1365.
- 65 Shannon, R. D. *Acta Crystallogr., Sect. A: Found. Crystallogr.* **1976**, *32*, 751–767.